# The Effects of Selective Doping on Electron Transport in Two-Dimensional Electron Gases

Thesis by

Ben Andrew Olsen

In Partial Fulfillment of the Requirements

for the Degree of

Bachelor of Science

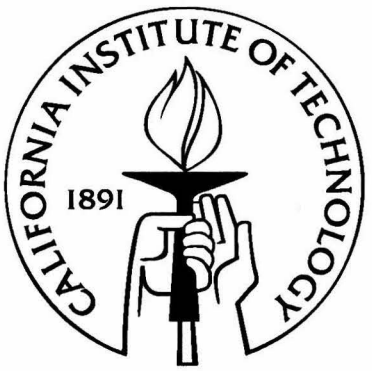


California Institute of Technology

Pasadena, California

2006

(Submitted May 1, 2006)

# Acknowledgements

I hardly know how to begin thanking everyone who has assisted me in my research. First and foremost, I'd like to thank Jim Eisenstein for going out on a limb and welcoming me into his lab, and for providing me a project I could sink my teeth into and spend an entire year on. Jim's matter-of-fact advice (both on matters in the lab and out) has helped me put a number of important issues in context, and has given me a greater perspective on what science really is.

Next, I would like to thank Ghislain Granger, who has been an endless source of information and encouragement this past year. Ghislain was always happy to double-check my work, brainstorm with me, or just keep me company during long data runs. I would also like to thank Lisa Tracy, for sharing her immense working knowledge of the lab, and Alex Champagne, for always giving me a second opinion. My first experience working as a part of a research group has truly been a pleasure.

# Abstract

Recent research on bilayer two-dimensional electron gases (2DEG) indicates the possibility of excitonic superfluidity, though experiments have measured small dissipation due to motion of unpaired vortices. In regular superconductors, carriers flow without dissipation beacuse vortices are "pinned" by impurities. This research investigates the effects of C and Si dopants within the quantum well of a single quantum well 2DEG. These dopants are candidates for improving vortex pinning in bilayer 2DEG systems. Four C-doped samples, with dopant density ranging from $3.5 \times 10^{14}$ cm$^{-3}$ to $2.5 \times 10^{16}$ cm$^{-3}$, and one Si-doped sample, with $2.3 \times 10^{15}$ cm$^{-3}$ Si ions are studied by electron transport measurements as functions of magnetic field strength. We find that minima in longitudinal resistance as a function of filling factor $\nu$ are wider and offset towards lower $\nu$ in samples with higher doping. This widening and shift is shown by mimina up to a $\nu$ that decreases with increasing C dopant density, but is not observed at all for minima in the Si-doped sample.

# Contents

# Chapter 1

# Introduction

Over the past three decades, an entirely new branch of condensed matter physics has emerged, namely the study of low dimensional electron systems. Though semiconductors, the host for these systems, had been studied intensively for decades, the novel behavior they show in exotic circumstances were entirely unpredicted thirty years ago. The first surprising behavior, the integer quantum Hall effect (IQHE), has since been used to measure the ratio of fundamental constants to an accuracy of one part in $10^9$, and is now used as the standard for resistance [1]. Even more surprising than the IQHE was the discovery of the fractional quantum Hall effect (FQHE), which can be explained only in terms of exotic quasiparticles with fractional charge [2]. One area of research on low-dimensional electron systems investigates the properties of two interacting two-dimensional electron gases (bilayer 2DEGs) and the strange new behavior they exhibit[1].

The IQHE and FQHE arise when electrons are confined to move in a plane perpendicular to a strong magnetic field. This so called two-dimensional electron gas (2DEG) is achieved most commonly through band engineering in semiconductor devices (e.g. GaAs/AlGaAs), in which thin layers of different semiconducting compounds are stacked to create a specific potential landscape in one direction. At sufficiently low temperature, conduction electrons are confined to move in one layer or at an interface between layers. These layered semiconductors are referred to as heterostructures [3].

## 1.1 Heterostructures

The most common heterostructures in use for the study of 2DEGs are made from combinations of thin layers of GaAs and AlGaAs[2]. These two compounds are used because they have identical crystalline structure, yielding nearly perfect crystal interfaces. Smooth interfaces allow the confined electrons to move about more freely, and their behavior can then be studied in more detail. The two common methods of confining electrons to motion in two dimensions are depicted in Figure 1.1.

[1] Here we provide the minimum introduction to this rich field that is required to understand this research; for a more thorough introduction, see [3, 4], and for a more technical discussion, see [5, 6].

[2] This section was adapted from Ref. [7], in which Cooper provides an expansive introduction to the subject.

The first construction involves one layer of GaAs and one layer of AlGaAs with n-type (positively charged ion) doping (commonly Si) far from the interface. Once the dopants release electrons into the crystal[3], they create an attractive potential for the electrons. Normally, the electrons would simply migrate past the interface back to the positive ions, but at low temperature ($\sim$ 1 K), the Fermi energy of electrons in the crystal is low enough that they become trapped in the triangular well and are effectively confined to motion in a plane. The second construction traps the electrons in a layer of GaAs sandwiched between layers of AlGaAs in what is essentially a finite quantum square well.

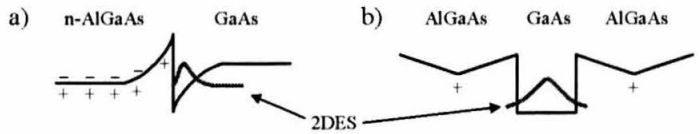


Figure 1.1: Band engineering to create a two-dimensional electron system. These diagrams depict the energy as a function of position in the heterostructure. After Reference [7].

### 1.1.1 Heterostructure Fabrication

Heterostructures are grown by molecular beam epitaxy (MBE), a process that has undergone considerable improvement in the past few decades. The most precise MBE processes can build crystal wafers one atomic layer at a time, with less than one part in $10^5$ impurities. To grow a heterostructure, a wafer of GaAs substrate in high vacuum is exposed to beams of molecules to create layers in the wafer. Before the delicate and sensitive quantum well for electron confinement is produced, a superlattice of alternating layers of GaAs and AlGaAs is grown on the GaAs substrate to smooth the surface and reduce the influence of any impurities (see Figure 1.2). On top of the superlattice, a thick layer of AlGaAs is grown. This layer includes a sheet heavily doped with Si ions to act as electron donors. Next, the quantum well depicted above (Figure 1.1b) is constructed, followed by another layer of AlGaAs with a dopant sheet. These dopants are included as a source for electrons, but are far from the quantum well to maintain the homogeneity of the crystal seen by the electrons (adding such dopants far from the 2DEG is referred to as delta doping).

## 1.2 The Quantum Hall Effect

The classical Hall effect, much more easily observed than its quantized counterpart, occurs whenever an electric current flows perpendicular to a magnetic field. Discovered in 1867 by Edwin Herbert

[3]This process is enhanced by illuminating heterostructures; captured photons allow electrons to overcome their binding energy to the Si dopants, and they can then migrate to the 2DEG. Though illumination is a common practice in quantum Hall system research, the details of the process are largely unknown (see [7, Ch. 3]).

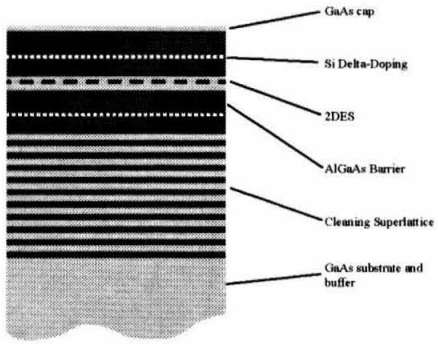


Figure 1.2: Layers of the heterostructure wafer used to observe the quantum Hall effect. After Reference [7].

Hall, the Hall effect describes a potential difference perpendicular to both the current and magnetic field lines, proportional to the strength of the magnetic field. In 1980, while studying Si field effect transistors, Klaus Von Klitzing of the Max Planck Institute for Semiconductor Research in Munich first observed the quantization of Hall resistance at various transistor carrier densities [8]. In his research, he varied the carrier density by changing the gate voltage on the transistor and observing various electron transport phenomena of the transistors at low temperatures and high magnetic fields. Most interesting was his observation that plateaus in the sample's Hall resistance occurred at resistances

$$R = \frac{h}{je^2} = \frac{25812.81\ \Omega}{j},$$

where $j$ is an integer, $h$ is Planck's constant and $e$ is the magnitude of the electron's charge. For his discovery of the quantization of the Hall voltage, Von Klitzing was awarded the Nobel Prize in Physics in 1985. More common in modern observations of the IQHE is the method of applying a fixed current to a sample with constant carrier density. The strength of the magnetic field is varied while measuring the potential difference between two points on the sample different from the current source and drain (see Chapter 4). Figure 1.3 shows typical results of such an experiment, displaying both the Hall resistance and the longitudinal resistance as functions of magnetic field strength.

### 1.2.1 Theory of the Quantum Hall Effect

Though a detailed explanation of the IQHE is only possible in the context of quantum mechanics, a semiclassical picture will expose most of the physical phenomena observed[4]. Consider a sheet of electrons within a heterostructure, essentially free to move in a plane, with a continuum of energies in the conduction band up to the Fermi Energy. Once a magnetic field is applied perpendicular to the plane of motion of the electrons, they move in circular paths with cyclotron radius $r_c$ inversely

[4]This section was adapted from Refs. [4, 5].

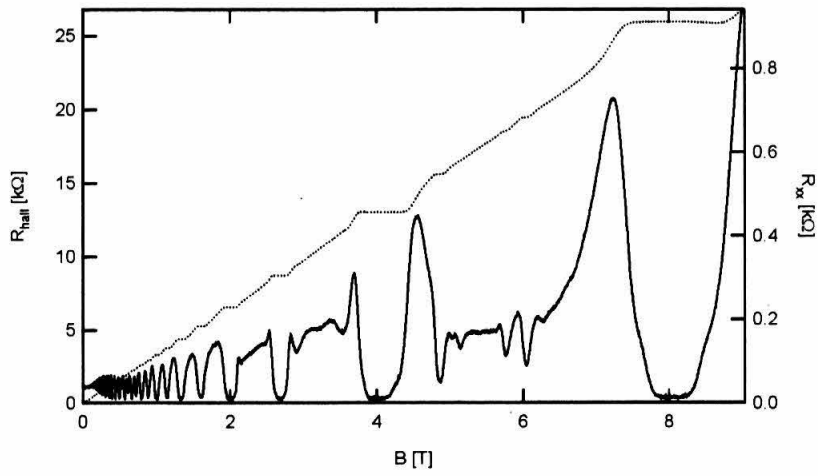


Figure 1.3: Sample Data obtained from a low-temperature heterostructure. The dotted trace represents the Hall resistance as a function of magnetic field strength (scale on left axis) and the solid trace represents the longitudinal resistance as a function of magnetic field strength (scale on right axis).

proportional to the strength of the field. The cyclotron radius is the classical radius at which an electron of given kinetic energy K and mass $m_e$ will orbit in a magnetic field of strength B, given by

$$r_c = \frac{\sqrt{2Km_e}}{eB}.$$

Due to the interaction between the electrons and the magnetic vector potential $\vec{A}$ in two dimensions described by the Hamiltonian

$$H = \frac{(p_x + eA_x)^2 + (p_y + eA_y)^2}{2m},$$

these radii will take discrete values, and the discrete energy levels corresponding to these radii are known as Landau levels. In two dimensions, the magnetic field will thus break the energy degeneracy of the Fermi sea into these discrete Landau levels. The degeneracy of these Landau levels is inversely proportional to the field strength, and can be estimated by dividing the area of the sample by the area of a cyclotron orbit. The ratio of independent electrons per unit area to magnetic field strength is constant and is equal to the ratio of fundamental constants $e/h$.

The plane of motion of the electrons necessarily contains some charged impurities. These impurities are closer to some electrons than to others, so the energies of states in each Landau level are spread out. In each Landau level, the highest and lowest energy states are spatially localized near impurities ("localized states"), and hence cannot conduct electric current macroscopically. The

electron states with energy

$$E \approx (n + \frac{1}{2})\hbar\omega_c, \text{ with } n = 0, 1, 2, \ldots$$

are extended spatially in the sample ("extended states"), and move about to conduct electric current. The number of electrons relative to the degeneracy of Landau levels is characterized by their ratio $\nu$. Essentially, the parameter $\nu$, called the "filling factor" describes the number of Landau levels that are filled with electrons. Changing the strength of the magnetic field will change the degeneracy of each Landau level, causing the most energetic electrons (those near the Fermi energy) to be either extended or localized. Thus, if the system is perturbed away from integer $\nu$ such that the states at the Fermi energy are localized, the macroscopic conductance will not change. This behavior leads to the plateaus in the Hall resistance at values of $h/je^2$ corresponding to $\nu = j$ integer filling factors.

Another important phenomenon evident in Figure 1.3 is the oscillation of the transverse resistance. Most importantly, the transeverse resistance is nearly zero over the range of magnetic field strengths associated with IQHE plateaus. To explain this feature, consider resistance as a rough measure of power dissipation within the sample. To dissipate power, an electron must transition to a state with lower energy, which is only possible if there is a nearby empty state to transition into. For magnetic field strengths at which the Hall resistance has plateaued, all the highest energy electrons are localized near impurities, and there exist no nearby states of lower energy to transition into. When the Fermi energy lies within extended states, however, the electrons may transition to lower energy states far away in the 2DEG. The behavior of the transverse resistance is known as Shubnikov-de Haas oscillation [3].

## 1.3 The Fractional Quantum Hall Effect

The 1998 Nobel Prize in Physics was awarded to Laughlin, Störmer, and Tsui for their discovery and explanation of the Fractional Quantum Hall Effect (FQHE)[5]. Störmer and Tsui were studying the IQHE in very pure heterostructures at very high magnetic fields. They discovered plateaus in the Hall resistance corresponding to filling factors of 1/3 and 2/3. These special states indicated that the charge carriers in the system acted as if they carried charge $e/3$. These quasiparticles were explained by the theoretical framework of a quantum liquid, proposed by Laughlin.

To understand the subtle quantum mechanical behavior of electrons near fractional filling factors, we consider a semiclassical picture of the two-dimensional electron gas. We imagine the viewpoint of one electron: it will have a probability density that varies over the plane of the sample. When the sample is placed inside a perpendicular magnetic field, the plane will be pierced by magnetic flux

[5]This section was adapted from Ref. [2].

quanta (discrete units of magnetic flux, the quantum analog of magnetic field lines, which produce dips in the wavefunction, called "vortices"(see Figure 1.4a) . If we consider the other electrons in the sample, they will coincide with the vortices (see Figure 1.4b). If all of the vortices produced by the flux quanta are filled by other electrons, the Landau level is filled. This state corresponds to the $\nu = 1$ integer quantum Hall state. If we then consider increasing the magnetic field by a factor of 3, then 3 times as many magnetic flux quanta will pierce the surface (see Figure 1.4c). It turns out that it is energetically favorable for an electron to "bind" more than one flux quantum rather than allowing the vortices created by the excess flux quanta to remain free. Thus, at $\nu = 1/3$, exactly three flux quanta pierce each electron (see Figure 1.4d).

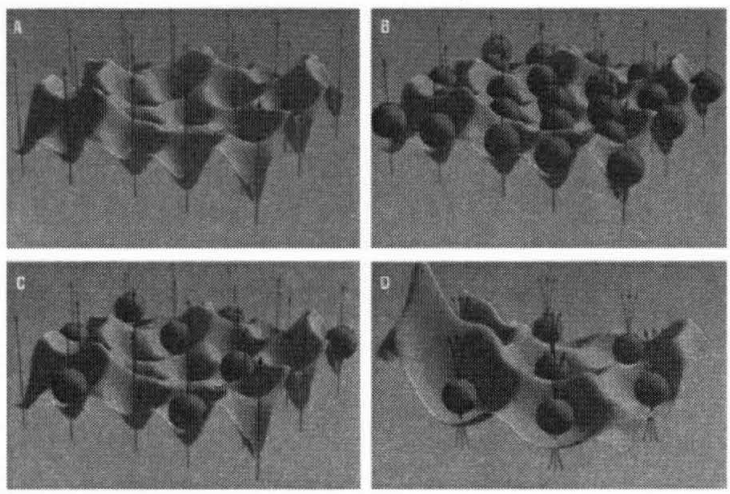


Figure 1.4: Representation of FQHE wavefunction. (a) Depiction the wavefunction of a single electron pierced by magnetic flux quanta. (b) Other electrons reside in the vortices. (c) For lower electron densities, some vortices are left unpaired. (d) A more favorable arrangement, pairing each electron with three vortices. This corresponds to the $\nu = 1/3$ fractional state. After Reference [2].

Deviation from this exact filling factor results in quasiparticles of charge $e/3$ appearing in the system, acting identically to electrons near the $\nu = 1$ IQHE state, except for a difference in charge (and, perhaps, in effective mass). In analogy to the IQHE, the FQHE plateaus and minima occur because these quasiparticles are localized by impurities in the crystal lattice and cannot conduct nor dissipate energy.

## 1.4 Bilayer Systems

If a heterostructure is grown with a pair of quantum wells near one another, the electrons trapped in one layer will interact with the neighboring electrons in both layers[6]. The strength of interactions with electrons in the other layer is determined by the layer separation, and can be made weaker

[6]This section was adapted from Ref. [1].

than, stronger than, or comparable to interactions with electrons in the same layer. As the interlayer separation is decreased, interactions between layers become stronger, and the electrons begin to tunnel between the two. This behavior is very sensitive to the layer separation, indicating that a phase transition occurs in the system for total filling factor $\nu_T = 1$ (i.e. $\nu = \frac{1}{2}$ in each layer, see Figure 1.5). The phase transition that occurs is the formation of excitons (bound electron-hole pairs). One can imagine simply exchanging empty electron states in the uppermost Landau level of one layer with positively charged holes, and exchanging electrons with empty hole states. This electron-hole transformation is completely consistent with semiconductor theory and permits analysis in terms of excitons, or electrons from one layer bound to the imagined holes in the other.

Excitons are normally created when an electron in a semiconductor is excited out of the valence band by absorption of light, leaving behind a hole to which it is attracted. The resulting exciton is unstable and quickly decays back into a valence electron by emitting light. The bilayer excitons described above exhibit much longer lifetimes, which permits more extensive studies on their behavior.

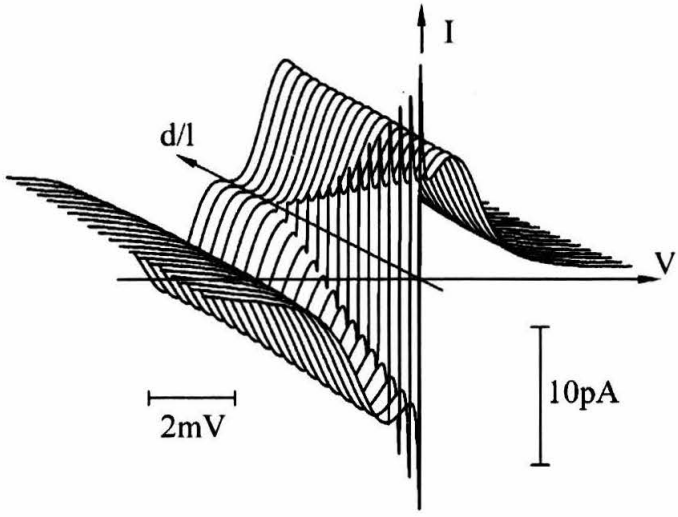


Figure 1.5: Interlayer tunneling in bilayer systems for a range of interlayer separations. Layer spacing is larger for traces at the back, and smaller for those at the front. The development of a near discontinuity suggests a phase transition, namely exciton formation. After Reference [10].

Since excitons are bound pairs of fermions (electrons and holes), they are compound bosons, and are hence not restricted by the Pauli Exclusion Principle. At very low temperature, therefore, a collection of excitons may all occupy the quantum ground state of the system. When the excitons all occupy the same quantum state, the phase of the wavefunction is coherent over many particles, and the quantum properties of the wavefunction become observable macroscopically. This phenomenon is known as Bose-Einstein Condensation.

In the bilayer 2DEGs described above, if the layers are spaced closely enough and the magnetic field strength tuned to give $\nu_T = 1$, Hall voltages (and hence Hall resistances) in both layers vanish (see Figure 1.6). To achieve this result, opposite currents are passed through the two layers. The vanishing Hall resistances indicate that no charged particles flow in either layer, implying that the electrons in one layer have all paired with holes in the other to form neutral excitons. This astonishing effect, along with the tunneling phase transition discussed above, suggest that the excitons form a Bose-Einstein Condensate.

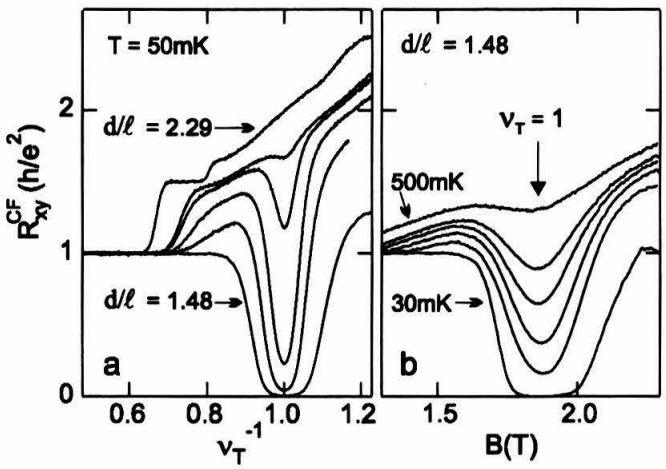


Figure 1.6: Vanishing Hall resistance ($R_{xy}$) caused by exciton formation. The left plot shows data taken at different interlayer separations, and the right plot shows data taken with fixed interlayer separation at different temperatures. This behavior suggests that the excitons form a superfluid. Some current research investigates whether this state is a Bose Einstein Condensate. After Reference [9].

Closely related to Bose-Einstein condensation is superfluidity: the flow of particles with vanishing dissipation. In a bilayer system, superfluidity would result in vanishing longitudinal resistance in both layers. The teams that have observed exciton condensation, however, have measured a small resistance where there should be none. This effect is due to the motion of unpaired vortices through the sample, which will dissipate energy when a current is applied [10]. In regular superconductors, dissipation due to vortex motion is eliminated by "pinning" the vortices, that is, localizing them near attractive defects in the material. In analogy, excitonic superfluidity would then be expected if one could localize vortices in a bilayer 2DEG. The most natural mechanism for localizing electrons and holes in a 2DEG system is to introduce impurities within the quantum well, such as C and Si ions. This research studies the effects of introducing impurities within a single quantum well 2DEG. Once the effects of selective doping are understood in the context of a single 2DEG layer, the study may be refined and advanced to bilayer systems.

## 1.5 Disorder in a Single Quanum Well

Though disorder is one of the major ingredients of the IQHE, it is not well understood to what extent impurities within the quantum well of the heterostructure will effect IQHE states. A simple explanation proceeds as follows: consider a system with exactly an integer number of Landau levels filled, and consider perturbing the system slightly by changing the magnetic field. If the field is changed to perturb the sample towards higher filling factor, the degeneracy of the Landau levels will decrease, and there will be a small excess of electrons. In the absence of any impurities, these extra electrons would conduct current macroscopically, and the sample would no longer be in an IQHE state. Now we introduce some positively charged impurities within this hypothetical sample (for example, some positively charged Si ions). The few excess electrons will be localized around these impurities, and will not contribute to macroscopic current within the sample, leaving it in an IQHE state. Thus, introducing Si ions into the quantum well is expected to widen the IQHE state in filling factor space towards higher $\nu$. Now, consider the reverse situation: start at an exact integer filling factor, and increase the field strength to decrease the filling factor in the sample. Instead of thinking of this situation as a depletion of electrons, we consider it as an excess of holes (the two views are mathematically equivalent). Then, the introduction of negatively charged impurities such as C ions will cause the excess holes to be localized and prevent them from contributing to macroscopic current. Thus, introducing C ion impurities into the quantum well should extend the IQHE states towards lower $\nu$. The extensions of IQHE states predicted by this model should be proportional to the number of impurities introduced, since more impurities will localize more electrons or holes.

This research tests the above prediction for electron/hole localization around charged impurities in the GaAs quantum well of a heterostructure. We test samples with Si or C dopants of various concentrations, introduced into the quantum well during the MBE fabrication process, by observing thier longitudinal resistances as functions of magnetic field. We expect to observe that the extension of the IQHE state is proportional to dopant concentration and occurs in only one direction in $\nu$-space.

# Chapter 2

# Experimental Method

## 2.1 Heterostructures

The devices used in this study were fabricated at Bell Laboratories in New Jersey using the MBE techniques described in the previous chapter. The heterostructures studied were grown specifically for the purpose of studying disorder in 2DEG systems, with either C or Si impurities intentionally mixed with the GaAs in an otherwise clean 300 Å quantum well. Introducing these impurities reduces the mean free path of the electrons in the 2DEG, reducing their mobility. The sample numbers, approximate doping level, and approximate mobility are summarized in Table 2.1. Of each wafer grown, only a small strip ($\sim$ 5 mm $\times$ 2 cm) was sent from Bell Labs.

| ***Sample*** | Dopant Concentration ($cm^{-3}$) | 2D $e^-$ Mobility ($cm^2/V\ s$) |
|---|---|---|
| 12-18-03.1 | $3.5 \times 10^{14}$ (C) | $3.8 \times 10^6$ |
| 12-9-03.1 | $2.8 \times 10^{15}$ (C) | $3.0 \times 10^5$ |
| 12-5-03.2 | $1.0 \times 10^{16}$ (C) | $6.5 \times 10^4$ |
| 12-31-03.1 | $2.5 \times 10^{16}$ (C) | $1.3 \times 10^4$ |
| 6-2-03.1 | $2.3 \times 10^{15}$ (Si) | $3.1 \times 10^5$ |

Table 2.1: The samples studied in this research. Introducing more dopants into the quantum well reduces the electron mobility, independent of dopant type. Nomenclature of samples indicates the date of fabrication, and the order of the wafer produced that day.

## 2.2 Sample Preparation

From each strip of wafer studied, a small square ($\sim 5 \times 5$ mm$^2$) is cleaved for wire-up[1]. To remove any surface impurities such as dust or residuals from the MBE process, each sample is gently scrubbed in an acetone bath, then rinsed in isopropanol and dried using a jet of nitrogen gas. The samples are observed under a microscope for any notable imperfections in the heterostructure surface (see, for example Figure 2.1) and recleaned if necessary. Once the surface of the samples are deemed

[1]This procedure, in large part, was adapted from the sample preparation procedure described in [11], where Spielman presents a rather extensive and detailed guide for a variety of processing methods.

suitably clean, small In contacts are soldered by hand to the corners and midpoints (see Figure 2.2) and annealed at 425°C for 5 minutes, during which time a constant flow ($\sim$ 2 standard liters per minute) of forming gas (15% $H_2$ gas, and 85% $N_2$ gas) passes through the annealing chamber. The annealing process causes the In contacts to diffuse into the heterostructure down to the level of the quantum well, creating an Ohmic contact. After annealing, $\sim$ 1" long, 0.001" diameter Au wire is soldered to each of the In contacts. The other end of each Au wire segment is soldered to a pin on an 18-pin plastic body header, to which the sample is attached using rubber cement. Since each sample only attaches to 8 of the pins, two samples are placed together on each header to allow for simulataneous cooling and measurement of the samples (see Figure 2.3).

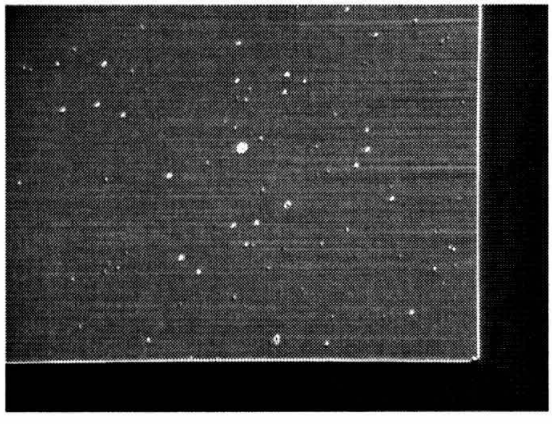

Figure 2.1: Sample 12-05-03.2A. The fine horizontal lines are artifacts from the wafer fabrication process, and the small dots are tiny surface defects. (Actual size: $\sim 1 \times 1$ mm$^2$)

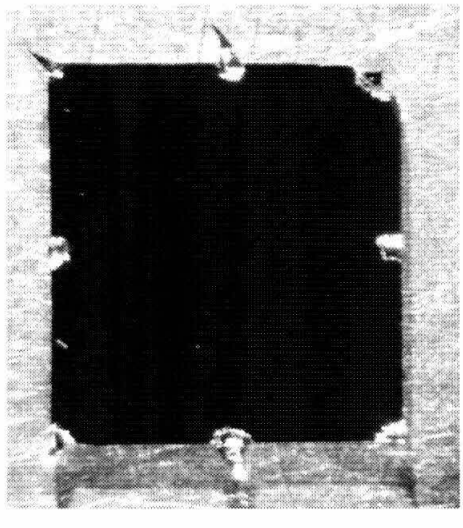

Figure 2.2: Sample 12-31-03.1A. This image shows the 8 hand-soldered In contacts before annealing. (Actual size: $\sim 5 \times 5$ mm$^2$)

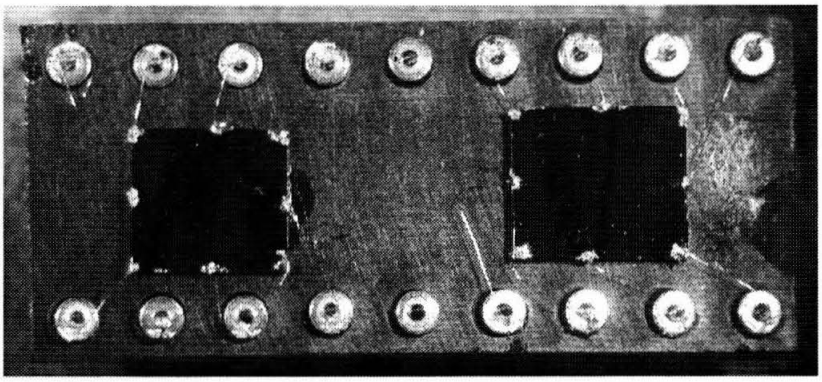

Figure 2.3: Practice Samples. These two pieces of scrap GaAs are wired up just like regular samples to refine the processing method. (Actual size: $\sim 3 \times 1$ cm$^2$)

## 2.3 $^4$He Dewar Dip Test

Once the samples are attached to headers, the contacts are tested at low temperature by dipping in liquid $^4$He (4.2K). Each header is attached to a dipstick, consisting of a sample chamber with a low-temperature GaAs light-emitting diode (LED) for illumination attached to a control box with 19 BNC connectors (18 for the header, and 1 for the LED) via a 1.5 m stainless steel tube (to allow for dipping into 60 L $^4$He dewars). The dipstick is lowered slowly to allow the sample chamber temperature to equilibrate with the liquid $^4$He. Eventually, the sample chamber is immersed and filled with $^4$He, then the sample is illuminated by passing a 1 mA current through the LED for 30 s (see circuit, Appendix A.1). After illumination, each contact is tested and its resistance compared with standard resistors (see circuit, Appendix A.2). If too many contacts are bad (having resistance much bigger than $\sim 1$ k$\Omega$), the sample is reannealed and rewired according to necessity.

## 2.4 Top Loading $^3$He Cryostat

After testing each sample at 4.2 K, headers are inserted into the sample chamber of a cryostat dipstick, also with a low-temperature LED, at the end of a 6 m stainless steel stick with a cable interface at the opposite end. The stick is attached to the top of the $^3$He Cryostat and pumped to near vacuum ($\sim$ 60 mTorr), which takes about an hour[2]. During this time, the pressure in the inner vacuum chamber (IVC) of the cryostat is checked and residual gas is pumped if necessary using a diffusion pump. The stick is also connected to an electronics rack with BNC connectors for each pin and for the LED during this time. During the lowering process, all the pin connectors are kept grounded, and a sliding seal on the stick is pumped (the inner chamber of the stick, which is connected to the inner chamber of the cryostat, containing $^3$He, is not pumped). Once the stick

[2]Most of the times and parameters used in operation of the cryostat are approximate, and were recommended by colleagues in the lab. Each experimenter will usually develop unique parameters.

reaches vacuum, the gate valve separating the stick from the inner cryostat chamber is opened, and the stick lowered slowly. During lowering, the sorb (a piece of activated charcoal with a heater and $^4$He cooling system) containing $^3$He is heated to release gaseous $^3$He to allow temperature equilibration between the stick and the $^4$He bath. Once the stick is fully lowered, the 1 K pot is filled with $^4$He and pumped, and the sorb is heated to liberate more gaseous $^3$He to allow the sample chamber to reach $\sim$ 1 K. After one hour of heating the sorb and cooling the sample chamber, the sorb heater is turned off to allow the $^3$He to condense, cooling the sample to 300 mK. During the condensation process, the sample is illuminated with the LED for 30 s (see circuit, Appendix A.1) Under ideal circumstances, this procedure keeps the sample at low temperature for eight hours.

## 2.5 Data Acquisition

Once the sample reaches 300 mK, the lock-in amplifier is attached to the stick's electronics with BNC cables for four-point measurements (For a single lock-in configuration, see circuit, Appendix A.3. For two lock-in configuration, see circuit, Appendix A.4.). The sample is fed an alternating current of $\sim$ 100 nA (rms) at 13 Hz (chosen so that 60 Hz line noise will not be detected by the lock-in as a harmonic of the signal). The magnetic field perpendicular to the 2DEG is produced by a superconducting magnet which is swept between 0 T and 9 T. As the magnetic field is swept, the output of the temperature sensor, the current through the magnet, and the output of the lock-in(s) are read by computer using a LabView routine written by Ian Spielman. The most rapid field sweeps take one hour (to prevent heating by the magnet). The data are output as plain text files and are given filenames identifying the date the sweep was taken as well as the system it was taken on, and which data sweep during the day it was (for example, "21feb06b.003" refers to the third data sweep taken using the $^3$He cryostat on February 21st, 2006).

# Chapter 3

# Data

In this chapter we present plots of longitudinal resistance ($R_{xx}$ or $R_{Long}$) as a function of perpendicular magnetic field strength. For each sample tested, only one representative trace is reproduced. For each sample tested, between 2 and 8 pin configurations are tested, with some pin configurations tested multiple times (sweeps from 0 T to 1 T with the same pin configurations, and sweeping the magnetic field both up and down). In most cases, $R_{xx}$ as a function of magnetic field strength appears the same for all pin geometries, with slight shifts in sample density and magnitude of resistance. Sample 12-05-03.2A exhibits strange behavior at $\nu = 2$ dependent on field sweep direction, so extra plots are shown for that sample.

In this chapter, filling factors $\nu$ are inferred by the approximate magnetic field. Since all of the samples tested have approximately the same electron density, an IQHE state will occur at roughly the same field strength for all samples. $\nu$ is determined by examining Hall resistance as a function of magnetic field (for example, Figure 1.3). For all the samples tested, $\nu = 1$ occurs at $\sim 9$ T, $\nu = 2$ at $\sim 4.5$ T, $\nu = 3$ at $\sim 3$ T, and so on.

## 3.1 Sample 12-18-03.1A (Low C-doping)

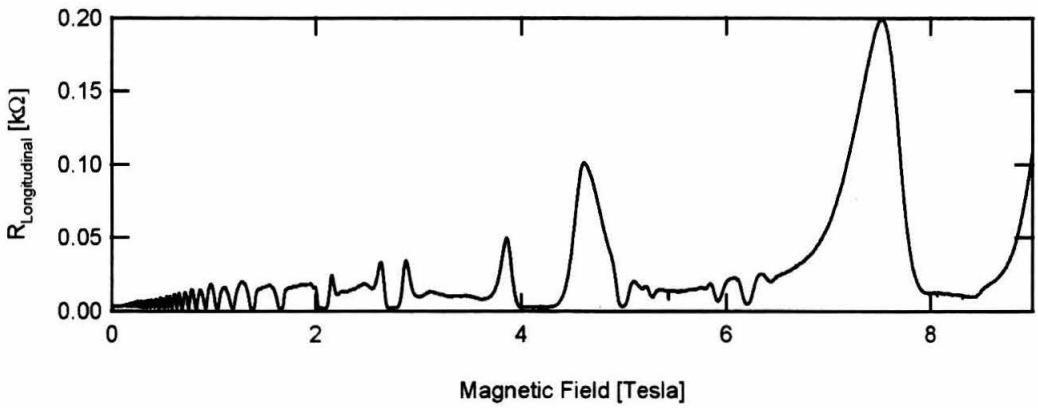


Figure 3.1: A plot of longitudinal resistance ($R_{Longitudinal}$) as a function of magnetic field strength for sample 12-18-03.1A.

The longitudinal resistance of sample 12-18-03.1A (see Figure 3.1) demonstrates characteristics common to high-mobility samples: a small magnitude resistance, well-resolved Shubnikov-de Haas oscillations even at very low field ($\sim$ 0.5 T), and fairly clear FQHE states at high field ($\sim$ 2.5 T corresponding to $\nu = 7/2$, $\sim$ 3.5 T corresponding to $\nu = 5/2$, and $\sim$ 5-6 T corresponding to $\nu = 5/3$, $7/5$, and $4/3$). The $\nu = 1$ minimum at $\sim$ 8 T does not reach zero resistance, and it exhibits a strange shape, though this effect is small. Additionally, spin-splitting (resolved odd filling factor peaks) appears at very low fields ($< 1$ T).

## 3.2 Sample 12-09-03.1A (Medium C-doping)

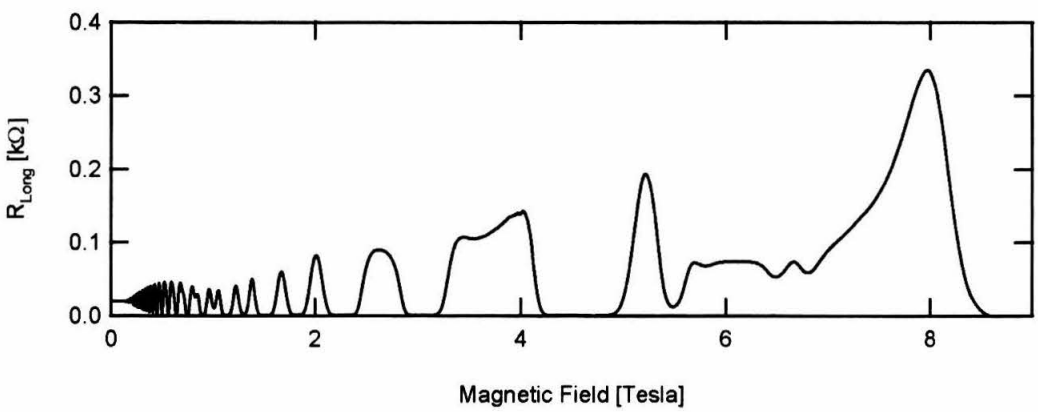


Figure 3.2: A plot of longitudinal resistance ($R_{Long}$) as a function of magnetic field strength for sample 12-09-03.1A.

Sample 12-09-03.1A exhibits some of the characteristics of a high-mobility sample (see Figure 3.2), though not as clearly as the previous sample. The magnitude of the resistance is roughly 4 times greater than that of sample 12-18-03.1A, as would be expected since the mobility is lower. Also, minima due to fractional states are present, but only at high fields ($\sim$ 6 T corresponding to $\nu = 5/3,\ 7/5$, and $4/3$). The minima at medium fields appear wider for this sample than those for sample 12-18-03.1A, and the spin splitting becomes resolved at $\sim$ 1 T.

## 3.3 Sample 12-05-03.2A (High C-doping)

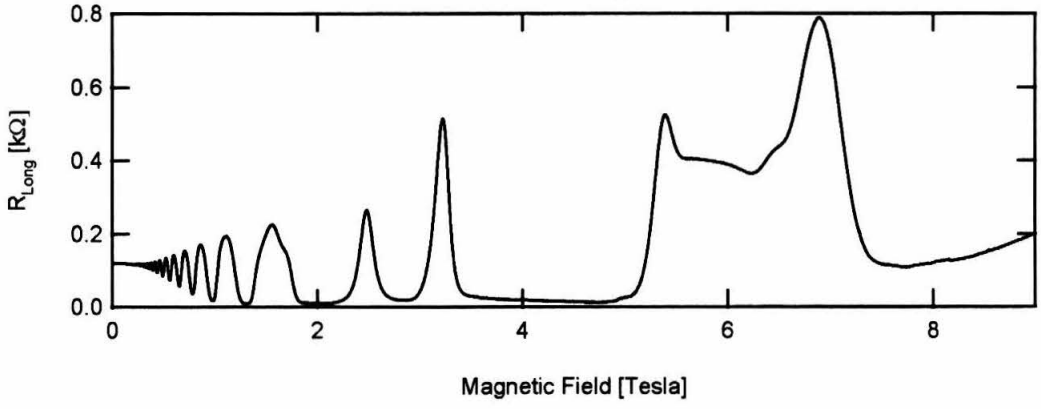


Figure 3.3: A plot of longitudinal resistance ($R_{Long}$) as a function of magnetic field strength for sample 12-05-03.2A.

Sample 12-05-03.2A (see Figure 3.3) shows very few of the features of the first two samples: though the magnitude of the resistance is about the same as sample 12-09-03.1A, the resistance at zero field is higher. Also, minima due to FQHE states are essentially noinexistent. Moreover, the only spin-split peak is at $\nu = 3$. The minima at high field appear wider than those of sample 12-09-03.1A.

Sample 12-05-03.2A also exhibits strange hysteretic behavior near $\nu = 2$. Depending on the direction of magnetic field sweep, the longitudinal resistance will either decrease (for increasing field strength) or increase (for decresing field strength), independent of field sweep rate (see Figure 3.4). The magnitude of this effect varies with pin configuration, but its shape is very similar for all configurations. Of the traces for all the pin configurations tested for this sample, the trace in Figure 3.3 had the smallest magnitude hysteretic effect.

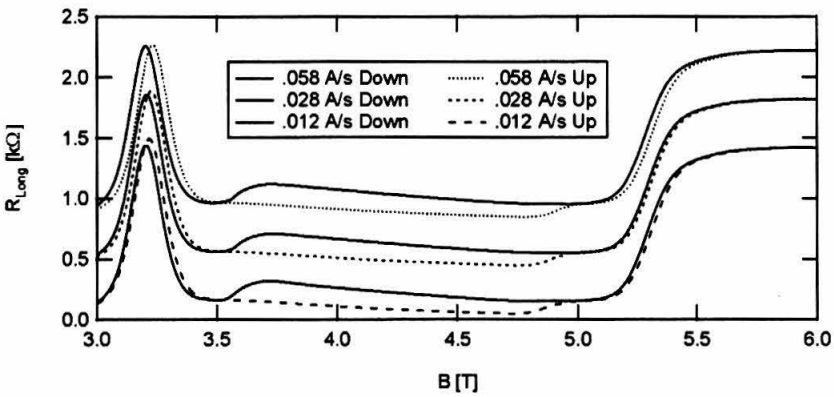


Figure 3.4: A plot of longitudinal resistance ($R_{Long}$) as a function of magnetic field strength for sample 12-05-03.2A. Strange hysteretic behavior at $\nu = 2$ appears independent of field sweep rate, and only dependent on sweep direction. In the plot legend, "A/s" refers to the ramp rate in the contacts of the superconducting magnet used to produce the field perpendicular to the sample, and "Up" and "Down" refer to increasing and decreasing magnet current, respectively.

## 3.4 Sample 12-31-03.1A (Very High C-doping)

Sample 12-31-03.1A (see Figure 3.5) exhibits the effect of large amounts of impurities within the quantum well very drastically: the magnitude of its longitudinal resistance is the largest of the samples, the minimum corresponding to $\nu = 2$ is zero over a range of 3 T with an average of $\sim$ 4.5 T, there is virtually no structure other than for even integer filling factors, and there are only 8 resolved minima in the trace. Another interesting feature present in this trace which is not discernible from Figure 3.5 is that the longitudinal resistance increases sharply as the magnetic field strength approaches 0 T, both as the field strength is swept upward and downward. Though this effect is very small ($\sim$ 50 $\Omega$), it is only observed in this sample.

## 3.5 Sample 6-02-03.1A (Medium Si-doping)

The behavior of sample 6-02-03.1A (see Figure 3.5) appears similar to that of sample 12-18-03.1A, but with a magnitude similar to that of sample 12-09-03.1A. There are well-resolved Shubnikov-de Haas oscillations at low field strength, and FQHE states at high field ($\sim$ 3.5 T corresponding to $\nu = 5/2$, and $\sim$ 5-6 T corresponding to $\nu = 5/3$, 7/5, and 4/3). Spin-splitting appears at very low fields, and almost all of the minima approach zero resistance.

From the data presented here, it appears that increased quantum well doping (both with C and with Si ions) generally increases the width of IQHE minima, decreases the number of resolved minima (both spin-split and non-spin-split), and increases the magnitude of $R_{xx}$. In order to quantify these effects better, further analysis is performed (see Chapter 4).

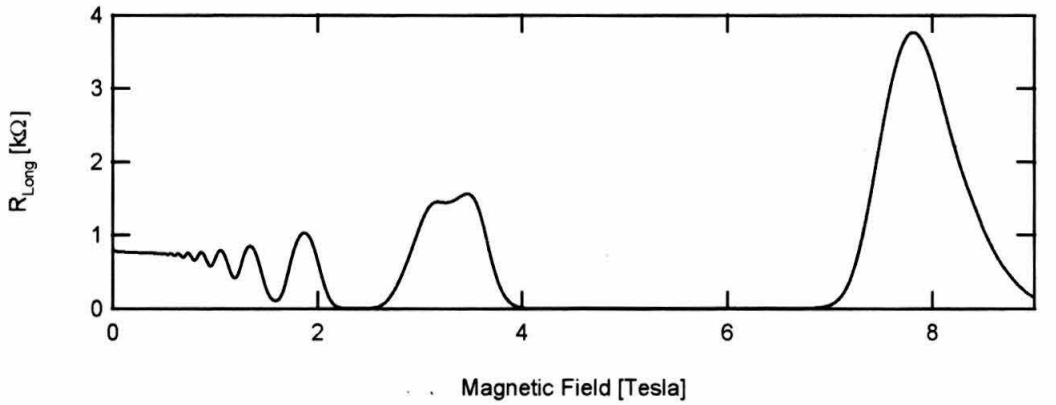


Figure 3.5: A plot of longitudinal resistance as a function of magnetic field strength for sample 12-31-03.1A.

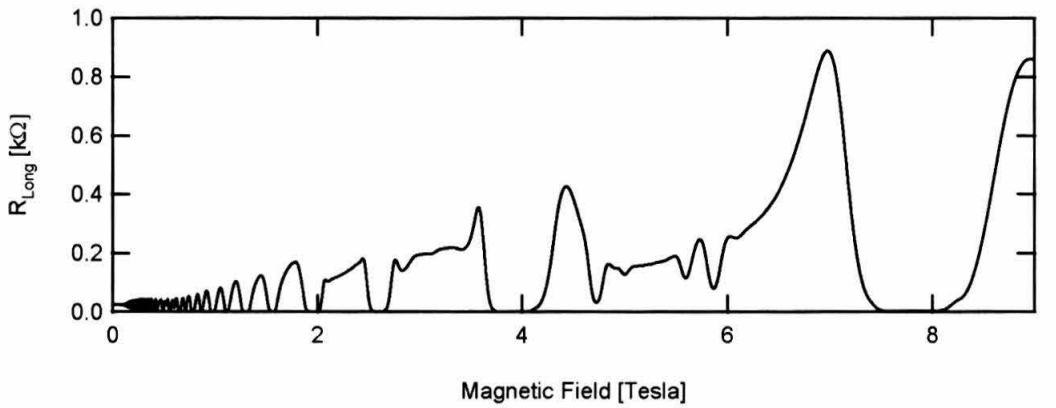


Figure 3.6: A plot of longitudinal resistance as a function of magnetic field strength for sample 6-02-03.1A.

# Chapter 4

# Data Analysis

Data analysis is carried out using the IGOR wave manipulation software[1]. Data are loaded from text files and appropriately scaled to produce waves representing longitudinal resistance as a function of perpendicular magnetic field. Minima in this wave are automatically computed and displayed with the wave so the user can appropriately modify the list of minima to remove erroneous minimum detections as well as minima associated with wide features in the resistance (see Figure 4.1).

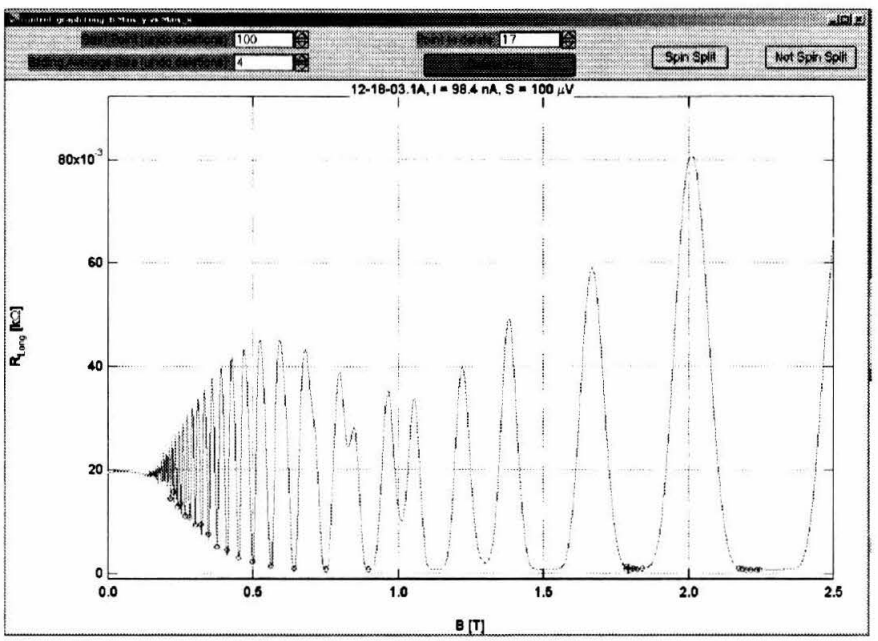


Figure 4.1: The first step of data analysis. A trace of resistance as a function of magnetic field is displayed as the solid line, and the computed minima are displayed as circles. At the top of the window are user controls for processing the minima, including start point to search for minima, a sliding box size for minima searching, and point deletion. A cursor is shown over the point selected for deletion.

[1]This procedure is automated as much as possible, requiring a minimum of time and effort to process the data. Not only did this save time during data analysis, but it also lead to greater consistency as well as ease of repeating part of the analysis. A sample of the code is reproduced in Appendix B.

The magnetic field of the minima in this wave are plotted against inverse filling factor $1/\nu$, with minima assigned an integer $\nu$ starting with a test factor of 8 and increasing by one for each successive minimum at lower magnetic field. To assign the correct test factor, the data with a linear fit are displayed on screen, with a user dialog to change the test $\nu$ and reperform the best fit. $\nu$ is then adjusted by hand until the linear regression and the data matches best, and the zero field offset in inverse $\nu$ is minimized (this corresponds to the correct $\nu$ values, see Figure 4.2). From the slope of the line is calculated the density of electrons $N_s$ in the 2DEG according to the formula

$$\frac{1}{\nu} = \frac{eB}{N_s h}.$$

Using this fit, a conversion between magnetic field and filling factor $\nu$ is calculated.

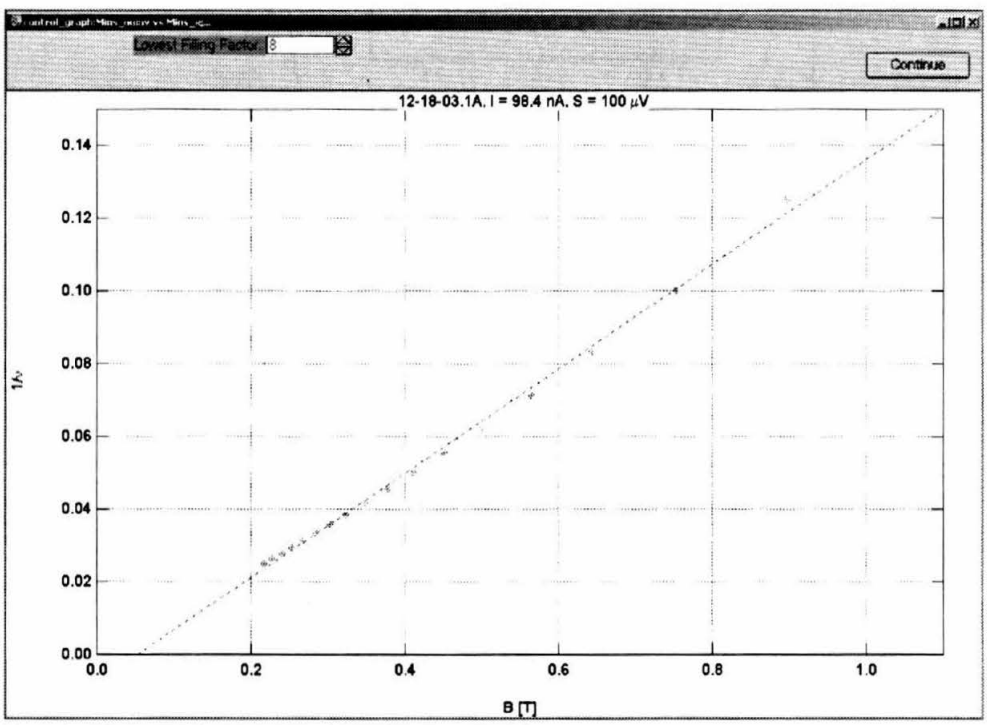


Figure 4.2: The second step of data analysis. Assigned inverse filling factor is plotted versus Magnetic field for each of the detected minima, with data shown in circles and the linear regression shown as a dashed line. The data shown here have been automatically assigned filling factors increasing from 8, which is incorrect since the data do not appear linear and the regression does not pass close to the origin. The correct filling factors for these data increase from 9.

A wave representing longitudinal resistance as a function of $\nu$ is then calculated, and the minima found automatically (and processed manually as before). The minima are then assigned $\nu$ values by hand, and the symmetry and shape of the minima are assessed as follows: at a user-defined level above the minima, both towards higher and towards lower $\nu$, are found "minima edges". The $\nu$ at

which the right edge (towards higher $\nu$), and the left edge (towards lower $\nu$) occur are averaged to find the "center" of the minimum. Uncertainty in edge detection is assessed by also detecting edges at 1/2 and 3/2 the defined edge level. This essentially gives the slope of the minimum edge (see Figure 4.3). The difference between the right and left edges is taken to calculate the "width" of the minimum. The $\nu$ of the center is compared to the assigned integer $\nu$ for each minimum to calculate the "offset" (see Figure 4.4). Finally, both offset and width as functions of $\nu$ are tabulated to be compared between samples.

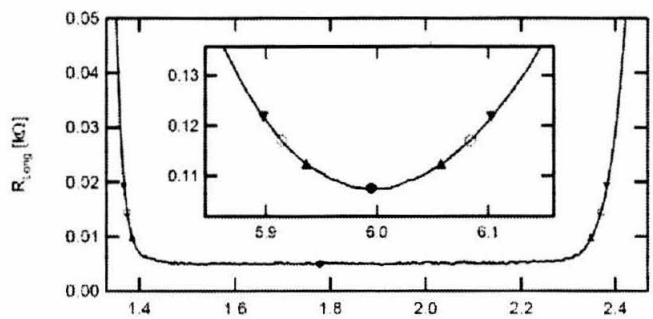


Figure 4.3: Two different minima and their detected edges for sample 12-31-03.1A. The filled circles are the detected minima, the empty circles are the edges detected at a user-defined level, and the triangles are upper and lower edges used for calculating uncertainty in edge position. As can be seen in the plot, detected minima don't necessarily occur at the center of the minima, especially for flat minima.

The IGOR analysis procedure is normally executed all at once, starting with the data input step, and carried through until the analysis for a given pin configuration is complete. All data and variables are stored in a data folder within the IGOR experiment, so they may be retrieved or modified later. The analysis procedure may also be restarted from one of four points requiring user input (recalculate the density, recalculate the conversion between B and $\nu$, refind minima, and reassign filling factors). This allows the user to correct mistakes without the need for redoing the entire analysis. Additionally, the user can create color or black and white versions of various plots with plot formatting performed automatically.

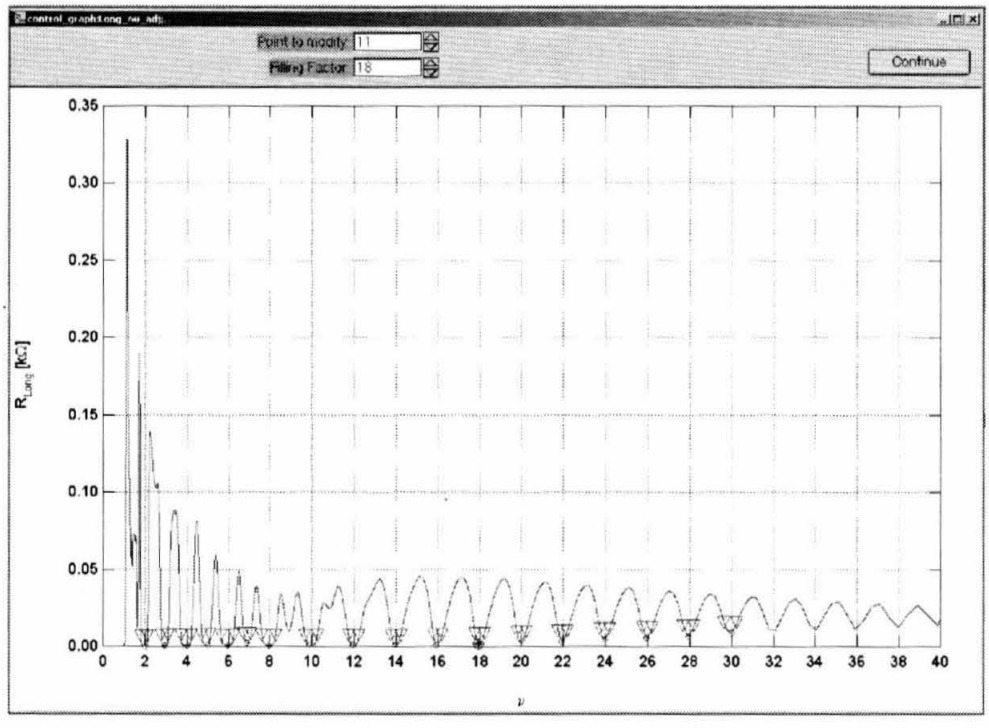


Figure 4.4: The final step of individual data analysis. A trace of resistance versus filling factor is displayed as a solid line, as well as the detected minima (circles) and left and right edges (triangles). Each minimum is then assigned the integer filling factor that it corresponds to, allowing computation of the minimum's offset and width in $\nu$.

# Chapter 5

# Results

In this chapter we present results of the analysis described in Chapter 4 for all of the samples tested. We provide plots of longitudinal resistance $R_{xx}$ as a function of filling factor $\nu$, as well as plots of minima width and minima offset as functions of $\nu$ for all the samples tested. These plots are meant to summarize the most important differences between samples caused by doping. For easier comparison, plots for the four C-doped samples are grouped together as follows: the plots of resistance as a function of filling factor for the four samples, followed by the four plots of minima width as a function of filling factor, then the plots of minima offset as a function of filling factor. Results for the Si-doped sample are provided in section 5.2.

## 5.1 C-doped Samples

### 5.1.1 $R_{xx}$ as a Function of $\nu$

In Figure 5.1 we show plots of $R_{xx}$ as a function of $\nu$ for all four C-doped samples. In Figure 5.1a, most of the features of sample 12-18-03.1A seen in Figure 3.1 are evident, but it can also be seen that the minima get wider and shallower with increasing $\nu$. The minima at low $\nu$ appear very narrow, in contrast to the wide minima seen in Figure 3.1, reflecting the nonlinear transformation between B and $\nu$. Additionally, spin-split (odd $\nu$) minima begin to appear at $\nu \approx 23$.

Figure 5.1b shows $R_{xx}$ versus $\nu$ for sample 12-09-03.1A. All of the minima appear wider than those in Figure 5.1a, and spin-split minima do not appear for $\nu > 11$. In general, $R_{xx}$ has fewer features for sample 12-09-03.1A than for sample 12-18-03.1A, though the minima at high $\nu$ appear more asymmetric.

Figure 5.1c shows $R_{xx}$ versus $\nu$ for sample 12-05-03.2A. The minima in this trace all appear wider, and become much shallower for high $\nu$, and the Shubnikov-de Haas oscillations almost disappear altogether. The only spin-split peak occurs at $\nu = 3$, and there is hardly any structure between minima. A slight asymmetry in the $\nu = 4$ minimum is evident.

Figure 5.1d shows $R_{xx}$ versus $\nu$ for sample 12-31-03.1A. Almost no features other than the minima at even $\nu$ are seen in this plot, with only a slight dip in the trace corresponding to $\nu = 3$. The Shubnikov-de Haas oscillations are only resolved for $\nu \leq 16$, where the oscillation is very small. The minima at $\nu = 2$ and 4 are the only minima with near zero resistance, and they are both very wide compared to minima in Figures 5.1a-c.

### 5.1.2 Minima Width and Offset as Functions of $\nu$

Figures 5.2 and 5.3 summarize the asymmetry in minima in $R_{xx}$ as a function of $\nu$ by quantifying the width and offset of the minima, respectively[1]. In both figures, different symbols represent different pin configurations or sweep directions, but the symbol for a given data sweep is the same in both figures. The error bars in both plots depict the error due to minima edge selection, not a statistical sample variance. As can be seen from 5.1, minima are not resolved at higher $\nu$ for some samples, but the axes on figures 5.2a-d and 5.3a-d are kept the same for easier comparison.

In figure 5.2a, the widths of the minima for sample 12-18-03.1A appear to increase linearly with $\nu$, with spin-split minima narrower than other minima. The former effect is due to the broadening of the minima seen in figure 5.1a, and the latter due to the fact that the spin-split minima are not, in general, as deep as the other minima. Figure 5.3a depicts the minima offset versus $\nu$ for 12-18-03.1A. The offsets appear to be zero for all $\nu$ except perhaps $\nu = 3$, though the offset is not significantly different from zero.

Figure 5.2b depicts minima width versus $\nu$ for sample 12-09-03.1A. Unlike in the previous sample, the widths do not increase with $\nu$. The even-$\nu$ minima increase for low $\nu$, then decrease to a constant width of $\sim 0.2$. There is a peak in width at $\nu \approx 8$, and the widths increase as $\nu$ is lowered below $\nu \approx 12$. Figure 5.3b shows the corresponding offsets for sample 12-09-03.1A. The spin-split minima are, in general, more offset towards lower $\nu$ than neighboring non-spin-split minima. For $\nu \geq 12$, the minima show no significant offset, but for $\nu < 12$, the offsets exhibit a hump in offset towards lower filling factor.

In figure 5.2c, the minima widths for sample 12-05-03.2A are shown. At high $\nu$, the widths increase rapidly with $\nu$, but for lower $\nu$, the minima exhibit odd behavior. With the exception of the spin-split $\nu = 3$ minimum (which is much narrower than the neighboring minima), the width of minima for $\nu \leq 4$ is roughly constant, then decreases until it reaches a minimum width at $\nu = 10$. The magnitude of these widths is almost twice as large as those for sample 12-09-03.1A. The corresponding offsets are displayed in figure 5.3c. Minima offsets for $\nu \geq 6$ are not significantly different from zero, and they are offset towards lower $\nu$ for $\nu < 6$, with the magnitude of offset greatest for the spin-split peak. The minima offsets for sample 12-05-03.2A are in the same direction as those in sample 12-09-03.1A, but greater in magnitude, and nonzero over a smaller range of $\nu$.

[1] See Chapter 4.

Figure 5.2d displays the minima widths for sample 12-31-03.1A, exhibiting the most extreme behavior of the four C-doped samples. For $\nu \geq 6$, the widths increase quadratically with $\nu$, and for $\nu \leq 6$, the widths decrease linearly with $\nu$. The magnitude of the greatest width is greater than that of sample 12-05-03.2A, and the $\nu$ at which the smallest minimum width occurs ($\nu = 6$) is less than that of 12-05-03.2A. The corresponding offsets shown in Figure 5.3d are equally extreme. The offsets for the minima at $\nu \geq 4$ are not significantly different from zero, and the offset of the minimum at $\nu = 2$ is about as large in magnitude as the greatest non-spin-split offset from sample 12-05-03.2A.

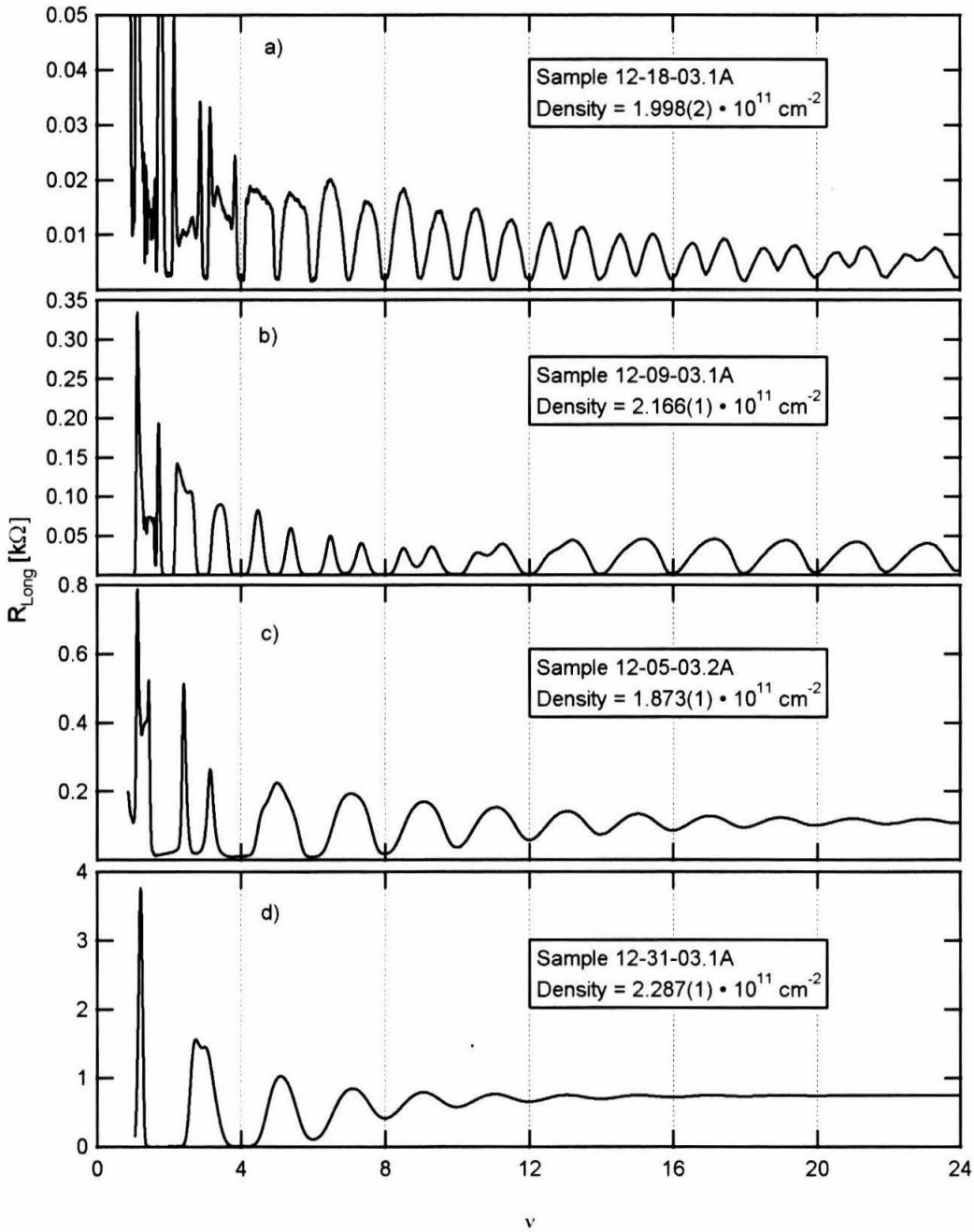


Figure 5.1: A plot of longitudinal resistance as a function of filling factor for all four C-doped samples. a) shows R vs. $\nu$ for sample 12-18-03.1A, b) for sample 12-09-03.1A, c) for sample 12-05-03.2A, and d) for sample 12-31-03.1A. The density listed in each legend, $N_s$, is the electron density calculated during analysis.

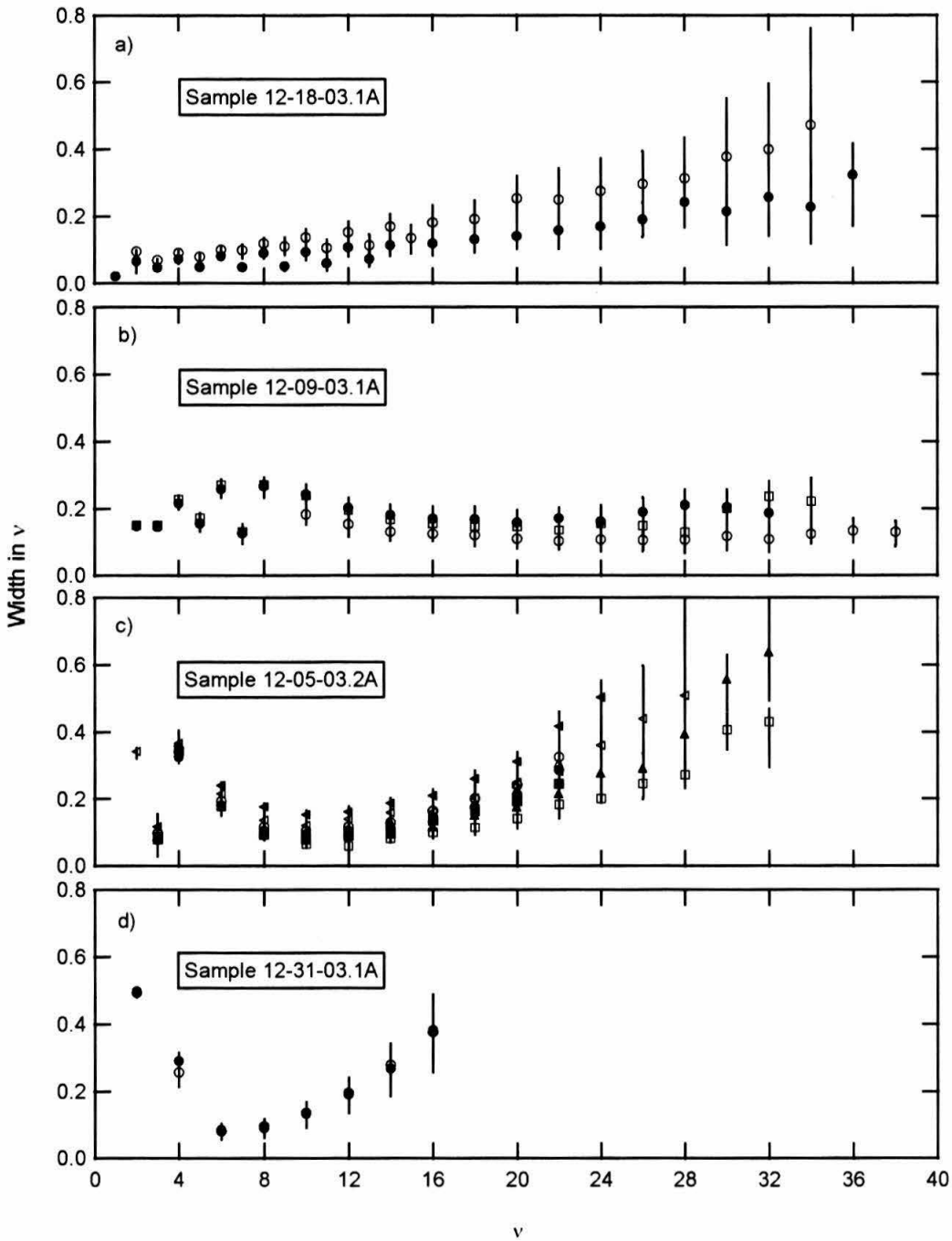


Figure 5.2: Minima width as a function of filling factor for all analyzed pin configurations for samples 12-18-03.1A (a), 12-09-03.1A (b), 12-05-03.2A (c), and 12-31-03.1A (d). Different symbols represent different pin geometries. Error bars are calculated from edge detections at 1/2 and 3/2 of the user defined level, and roughly correspond to the slope of the minima edges.

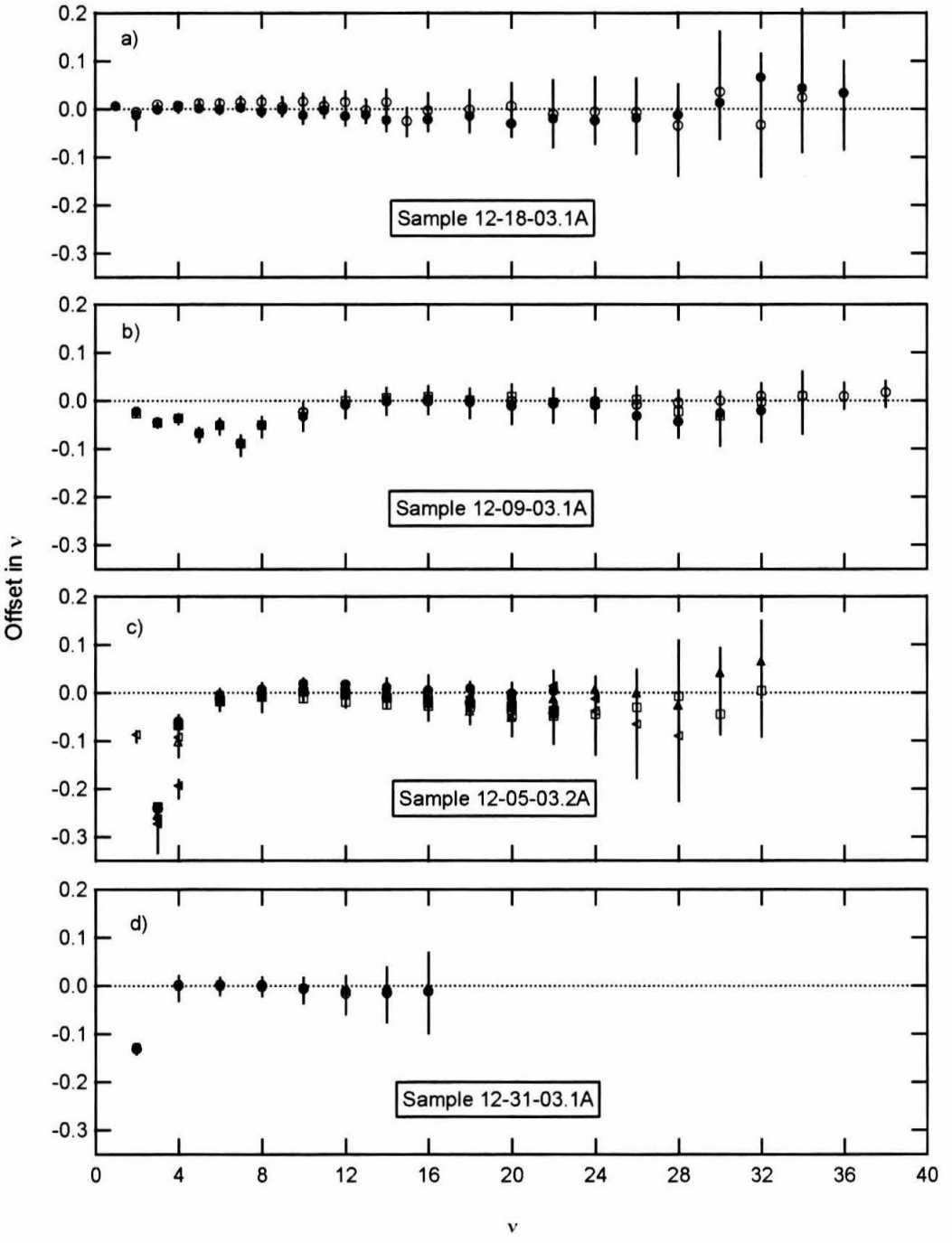


Figure 5.3: Minima offset as a function of filling factor for all analyzed pin configurations for samples 12-18-03.1A (a), 12-09-03.1A (b), 12-05-03.2A (c), and 12-31-03.1A (d). Different symbols represent different pin geometries. Error bars are calculated from edge detections at 1/2 and 3/2 of the user defined level, and roughly correspond to the slope of the minima edges.

## 5.2 Si-doped Sample

Figure 5.4 shows a plot of $R_{xx}$ versus $\nu$ for sample 6-02-03.1A. Qualitatively, this plot appears intermediate to Figures 5.1a and 5.1b. The minima widen slightly with increasing $\nu$ for low $\nu$, but remain the same width for large $\nu$. Minima widths appear to be wider than those in 5.1a and narrower than those in 5.1b. Spin-split minima begin to appear at $\nu \approx 17$, and minima seem slightly asymmetric, skewed opposite those of 5.1b.

Figures 5.5 and 5.6 summarize the minima widths and offsets, respectively, of sample 6-02-03.1A. The minima widths increase linearly for low $\nu$, then remain roughly constant for higher $\nu$. Qualtitatively ,this behavior seems similar to that show in Figure 5.2b without the peak at lower $\nu$. None of the minima offsets are significantly different from zero, similar to those in 5.3a.

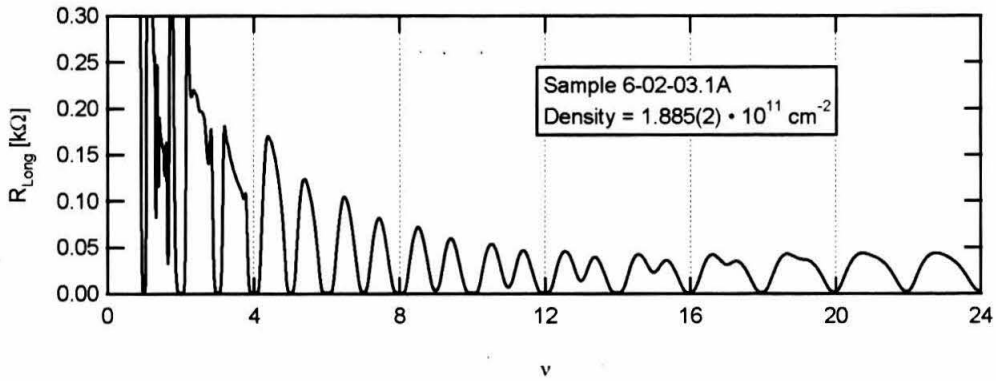


Figure 5.4: A plot of longitudinal resistance as a function of filling factor for sample 6-02-03.1A

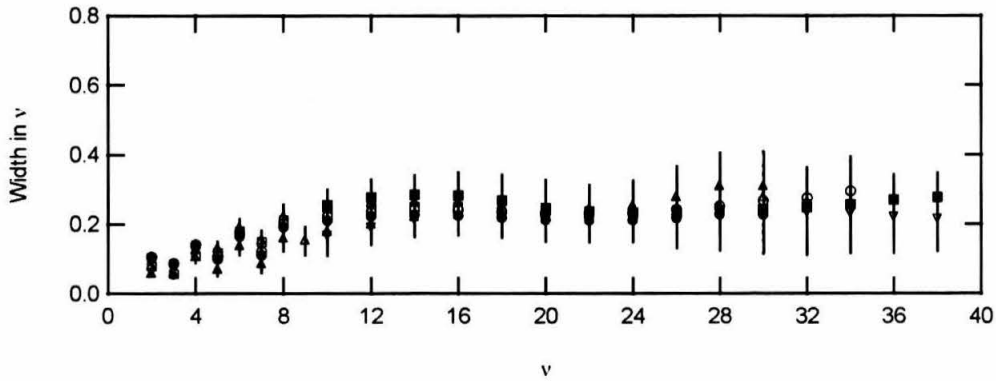


Figure 5.5: Minima width as a function of filling factor for all analyzed pin configurations for sample 6-02-03.1A. Different symbols represent different pin geometries. Error bars are calculated from edge detections at 1/2 and 3/2 of the user defined level, and roughly correspond to the slope of the minima edges.

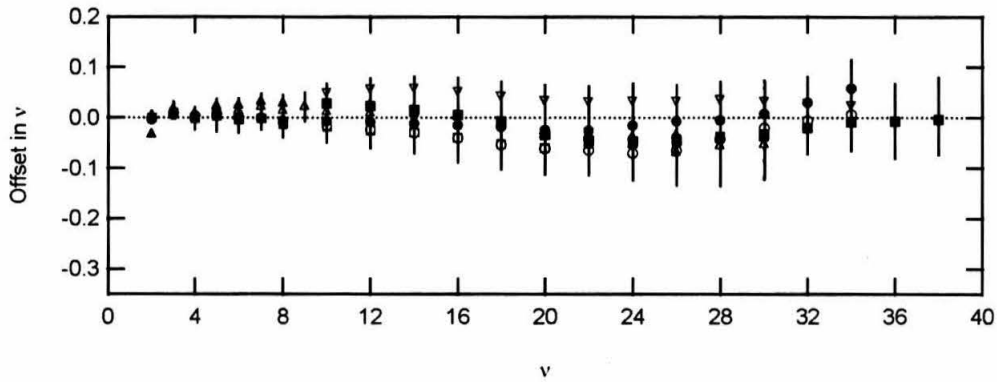


Figure 5.6: Minima offset as a function of filling factor for all analyzed pin configurations for sample 6-02-03.1A. Different symbols represent different pin geometries. Error bars are calculated from edge detections at 1/2 and 3/2 of the user defined level, and roughly correspond to the slope of the minima edges.

The results of the data analysis indicate that sample behavior is largely indpendent of pin configuration for this experiment. These results also quantify the effect of increased C ion dopant concentration on electron transport in a single layer 2DEG. As C ion concentration increases, minima in $R_{xx}$ at low $\nu$ generally widen and shift towards lower $\nu$. Additionally, Si doping at similar concentration has a much smaller effect on transport measurements.

## 5.3 Summary and Discussion

Summarized in Table 5.1 are the main results obtained for the five samples tested. The values in the table are meant to summarize the peaks observed in samples 12-09-03.1A, 12-05-03.2A, and 12-31-03.1A for minima with and offset in $\nu$. Since these peaks were not observed in samples 12-18-03.1A and 6-02-03.1A, no summary is provided. It appears that both the peaks in width and in offset have magnitude roughly proportional to dopant concentration, and width roughly inversely proportional to dopant concentration. Increased magnitude of minima width and offset with greater dopant concentration is precisely what we predicted in Section 1.5.

The increased magnitude of the effects with higher dopant concentration can be explained by considering the mobilities of charge carriers in the various samples. With increasing dopant concentration, the electron mobility and the hole mobility decrease (see Table 2.1 for approximate electron mobilities), reflecting a greater number of interactions between charge carriers and other objects per unit time[2]. If the excess charge carriers (in this case, holes) have lower mobility, they are more likely to be localized by a C ion.

[2]It is assumed here that electron mobility and hole mobility in a given sample are positively correlated, so that the tested samples with high electron mobilities will have high hole mobilities as well.

The decreasing range of the widening and shifting of minima can be explained by the "lifting" of the minima seen at lower $\nu$ for higher dopant concentration. Since the minima don't reach zero resistance, they don't spread out, and appear narrower and more symmetric. The fact that minima width and offset are changed much less for the Si-doped sample (6-02-03.1A) than for the C-doped sample with similar dopant concentration (12-09-03.1A) may be due to the much larger effective mass of holes than electrons in GaAs[3]. Since the electrons have a much lower effective mass, they will be less easily localized by impurities than holes, and the effects of the dopants on macroscopic transport will be smaller.

| ***Sample*** | Widest minimum | $\nu_{max}$ | Largest offset | $\nu_0$ |
|---|---|---|---|---|
| 12-18-03.1 | – | – | – | – |
| 12-9-03.1 | 0.28 | 14 | -0.10 | 12 |
| 12-5-03.2 | 0.34 | 10 | -0.25 | 8 |
| 12-31-03.1 | 0.50 | 6 | -0.13 | 4 |
| 6-2-03.1 | – | – | – | – |

Table 5.1: A summary of experimental results. Widest minimum is the widest minimum observed in the peaks at low $\nu$. $\nu_{max}$ is the maximum $\nu$ at which the peak in widths is observed (this quantifies the width in $\nu$-space of this effect). $\nu_0$ is the minimum $\nu$ after which all the minima are not significantly offset. Dashes for samples 12-18-03.1A and 6-02-03.1A reflect that no significant widening or offset of minima is observed.

[3]The effective mass of the electron in GaAs is 0.067 $m_e$, where $m_e$ is the mass of the electron. The effective mass of holes in GaAs is $\sim$0.45 $m_e$, though in heterostructures, it has been observed with different values. See Ref. [12].

# Conclusion

In this research we investigated the effects of introducing C or Si impurities within a single quantum well 2DEG. We observed that increased dopant concentration not only reduces the magnitude of longitudinal resistance $R_{xx}$, but also decreases the number and depth of minima in $R_{xx}$ as a function of perpendicular magnetic field strength. In the four C-doped samples tested, increasing dopant concentration widens the IQHE minima and offsets them towards lower $\nu$, but over a range of $\nu$ that decreases with increasing dopant concentration. We do not observe this effect in the Si-doped sample 6-02-03.1A, with dopant ion concentration similar that of sample 12-09-03.1A. This discrepancy is likely due to the difference in effective mass between electrons and holes in GaAs.

These results are promising. Future tests on samples with higher Si ion concentration will clarify the discrepancy between C and Si doping. We expect that samples with higher concentrations of Si ion dopants will exhibit similar behavior to the C-doped samples tested in this research. Once widening and offset are confirmed for samples with electron donor impurity ions like Si, an extension of this experiment to bilayer systems seems likely to reveal rich phenomena. If all goes well, future experiments may test the effects of dopant ion concentration and species on macroscopic exciton transport.

# Appendix A

# Circuits

## A.1 LED Illumination

The circuit depicted in Figure A.1 is used for illuminating samples both at 4.2 K in $^4$He dewars and at 1 K in the $^3$He cryostat. A voltage source is connected to the sample via a standard 1 kΩ resistor. The 1 kΩ resistor acts as a current meter for the LED: when the two voltmeters differ by 1 V, the current passing through the circuit is 1 mA. In practice, the voltage provided by the source is increased until the observed voltage difference between the two ends of the resistor is 1 V, then reduced after 30 s.

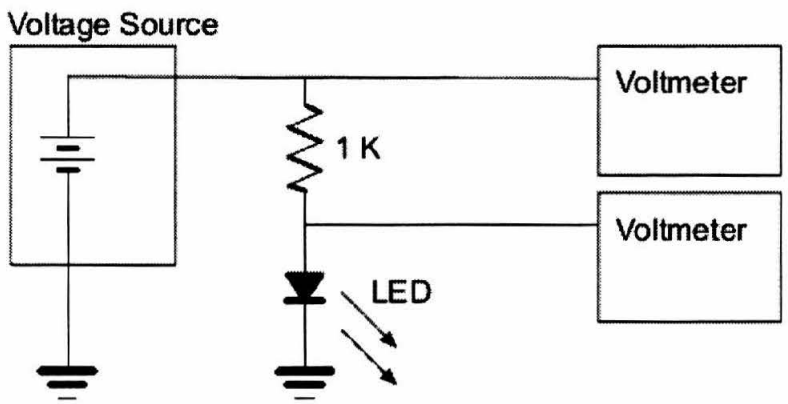


Figure A.1: The circuit used to illuminate the sample using a low temperature GaAs LED.

## A.2 Contact Testing

A simple method for testing if a contact is working is to measure the resistance of the contact and sample when all the other contacts are grounded. The circuit depicted in Figure A.2 is used to test the contacts of each sample at 4.2 K. The output of the Lock-in amplifier is fed through a voltage

divider consisting of a 511 Ω resistor and a 1 Ω resistor to ensure that the excitation voltage does not damage the sample. The output voltage $V_{out}$ is attached to the pin for a contact on the sample (all of the pins are kept grounded until tested) through a box of standard resistors (switched by a dial on the box). The current passes through the standard resistor, then through the sample to ground, so the circuit is essentially another voltage divider. The voltage difference across the standard resistor is measured, and the sample resistance calculated using the formula

$$R_{sample} = R_{box}(\frac{V_{in}}{V_{out}} - 1).$$

Good contacts have $R_{sample} \approx 1k\Omega$, and bad contacts usually have resistances greater by an order of magnitude. If one or two out of eight contacts are bad, the sample may still be tested, depending on which contacts are bad.

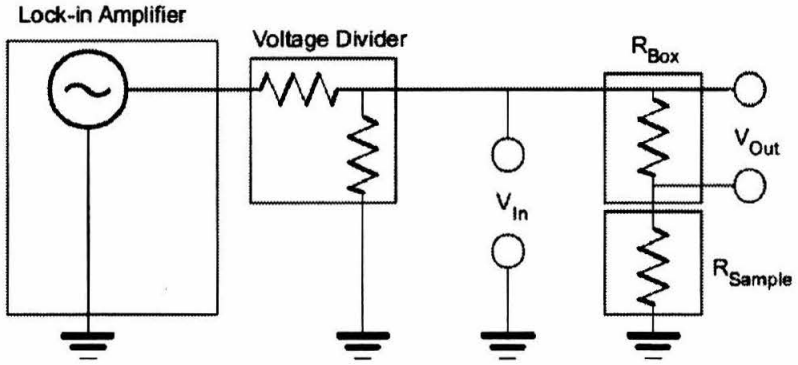


Figure A.2: The circuit used to test sample contacts. $R_{Box}$ is a set of known resistances that are selected with a knob. The component of $V_{out}$ at the same frequency as the output signal is measured by the Lock-in.

## A.3 One Lock-in Four Point Measurement

The circuits depicted in Figure A.3 are used to make most of the measurements of $R_{xx}$ (Figure A.3a) and $R_{Hall}$ (Figure A.3b) as functions of magnetic field. The output of the Lock-in amplifier is sent through a 10 MΩ resistor to effectively convert the voltage source into a current source, since the impedance of the sample is much less than 10 MΩ. This output current is measured using a current amplifier which outputs a signal proportional to the current. To make a four point measurement, the current output is attached to the drain pin, a shorting cap to the source pin, and two BNC cables connecting the voltage measurement pins to the input of the lock-in measurement stage (all pins are grounded during connections). Then, all the pins are floated (disconnected from ground),

and the current ramped up slowly. The output frequency of the lock-in is set at 13 Hz, and the measurement frequency is set to $\sim$ 13 Hz, but varied (typically by $\sim$ 0.3 Hz) to maximize the signal for a given measurement. The phase offset of the output and measurement stages is also adjusted to correct for capacitive elements in the circuit. This is done by offsetting the phase of the signals by 90 degrees, and adjusting the phase offset so that the measured signal vanishes. The 90 degree offset is then removed for making measurements.

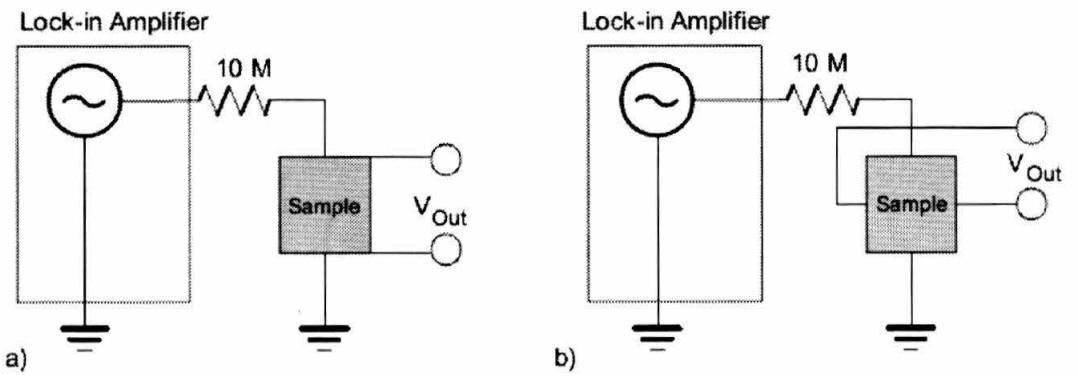


Figure A.3: The circuits used to measure samples. In (a), the circuit measures longitudinal voltage (to calculate $R_{xx}$), and in (b), the circuit measures Hall voltage (to calculate $R_{xy}$). The component of $V_{out}$ at the same frequency as the output signal is measured by the Lock-in.

## A.4 Two Lock-in Measurement

In general, the two Lock-ins are used independently to measure $R_{xx}$ on two different samples simultaneously. In the cases where only one sample is cooled at once, however, both Lock-ins may be used to simultaneously measure $V_{xx}$ and $V_{Hall}$ for a single sample. The output of Lock-in A is sent to the reference channel of Lock-in B to match the frequency, so that the two may measure voltages corresponding to the output current of Lock-in A. For details on preparation of the Lock-in circuit, see Section A.3.

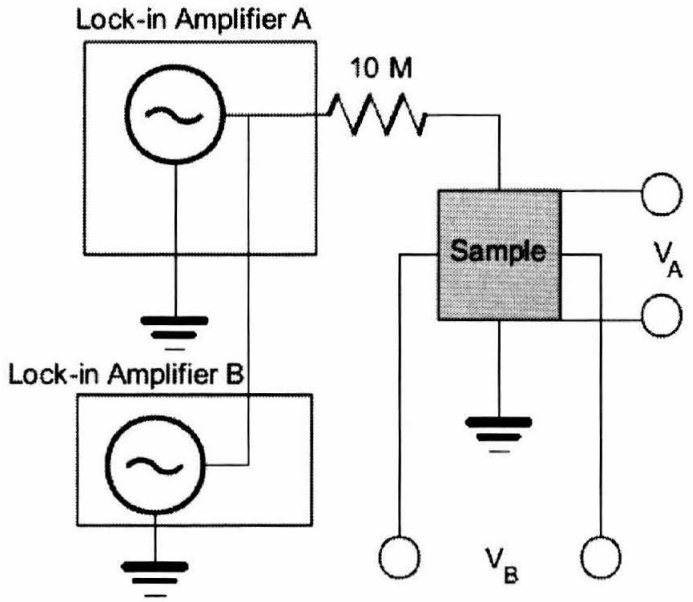


Figure A.4: The circuit used to measure both longitudinal and Hall voltages simultaneously. The line connecting the two Lock-in voltage sources represents the reference signal for Lock-in B. The components of $V_A$ and $V_B$ at the same frequency as the output signal of Lock-in A are measured by Lock-ins A and B, respectively.

# Appendix B

# IGOR Data Analysis Code

In this section, we present samples of the IGOR analysis code used to analyze raw data. This code is saved as an IGOR procedure file, and called from within an IGOR experiment (an environment in which data is manipulated) using a macros menu. Data are loaded from a text file and stored as waves (lists that can be assigned units and scaled in both independent and dependent variables) in data folders contained within the experiment.

## B.1 Density Calculation

This code is used to calculate the electron density for the sample data, using a wave of inverse filling factor as a function of magnetic field. The linear regression used to obtain the value for the density is also used to create a wave representing longitudinal resistance as a function of filling factor. The beginning of the code contains initialization procedures, so that waves created in previous analysis can be loaded into the analysis environment. After initialization, a user interactive window is activated to display both the wave of detected minima and the linear regression, with a field to change the assigned filling factors. Following that is the code that creates a new wave representing resistance as a function of filling factor.

```
//Calculates the density from a plot of 1/nu vs. B to map waves to R vs. nu
      Duplicate /O Mins_x, Mins_nu
      Variable i = 0, j = 8   //Default initial nu value

      For(i = DimSize(Mins_nu, 0); i > 0; i -= 1)
         Mins_nu[i - 1] = j
         j += SS_coeff
      Endfor

      Duplicate /O Mins_nu, Mins_nuinv
```

```
	Mins_nuinv = 1 / Mins_nu
	Make /D /O /N = 2 Mins_coeff   //Variables for linear fit
	Duplicate /D /O Mins_x, Mins_fit
	CurveFit line kwCWave = Mins_coeff,  Mins_nuinv /X = Mins_x /D = Mins_fit
	Mins_fit = Mins_coeff[0] + Mins_coeff[1] * x
	Wave W_sigma = W_sigma //creates local reference to wave

//*********Control window for adjusting filling factors**************
	Display /W = (0,0,850,600) Mins_nuinv vs Mins_x
	ModifyGraph mode(Mins_nuinv)=3, marker=42, rgb(Mins_nuinv)=(19456,39168,0)
	ModfiyGraph msize(Mins_nuinv) = 2,mirror=1,standoff=0
	Label left "1/\\F'symbol'n\\F'arial'"
	Label bottom "B [T]"
	SetAxis/A/E=1/N=1 left
	SetAxis/A/E=1 bottom
	AppendToGraph Mins_fit
	ModifyGraph rgb(Mins_fit)=(0,0,65280), lstyle(Mins_fit)=3, grid=1,tick=2
	SetAxis left 0,0.15
	SetAxis bottom 0,1.1
	TextBox/N=myTitle/F=0/A=MC/X=3/Y=48.4/E title
	Variable /G nu_start = 8
	Variable density = 1.6022/6.626068/Mins_coeff[1], offset=Mins_coeff[0]
	ControlBar 70   //Window controls
	SetVariable setFilling,pos={200,5},size={200,30},proc=FullSetFilling
	SetVariable title="Lowest Filling Factor:"
	SetVariable setFilling,labelBack=(32768,40704,65280), fSize = 16
	SetVariable setFilling,limits={0,100,1},value= nu_start,bodyWidth= 100

	Button finishMins,pos = {1000,25}, size = {120,30},proc=FullFinishWindow
	Button finishMins,fColor=(32768,65280,32768), fSize = 16,title="Continue"

	DoWindow /F /C control_graph //Allows user to use window controls
	PauseForUser control_graph   //until Continue button is pressed

	Variable /G sig_dens = 1.6022 / 6.626068 / Mins_coeff[1] ^ 2 * W_sigma[1]
	Variable sig_off = W_sigma[0]
```

```
      density = 1.6022 / 6.626068 / Mins_coeff[1]
      offset = Mins_coeff[0]
      String /G Mins_legend = "\\s(Mins_nuinv) Minima\r\\s(Mins_fit) Linear Fit"
      String /G Mins_info = "e/Nh = " + num2str(Mins_coeff[1]) + "  "
      Mins_info += num2str(W_sigma[1])+ " T\\S-1\\M"
      Mins_info += "\rN\\Bs\\M = "  + num2str(1.6022 / 6.626068 / Mins_coeff[1])
      Mins_info += "  " + num2str(1.6022/6.626068/Mins_coeff[1]^2*W_sigma[1])
      Mins_info += "  10\S11\M cm\S-2" + "\r\\F'symbol'n\\F'arial'\\Boff\\M = "
      Mins_info += num2str(Mins_coeff[0]) + "  " + num2str(W_sigma[0])
   EndIf

//*****************************************************Convert from B to nu***
//Creates a wave of R vs. nu using the calculated density
   If(doNuAdj == 1)
      If(doDensity == 0) //Initialize Variables, strings and waves
         NVAR wave_length,density,offset,new_density,new_offset,sig_dens,sig_off
         SVAR title
         Wave Long_wave, B_wave, W_sigma
      EndIf

      Variable /G new_density = density, new_offset = offset
      Print density, new_density
      Duplicate /O Long_wave, Long_wave_copy
      Duplicate /O B_wave, Nu_wave
      Nu_wave = min(abs(1 / (1.6022/density/6.626068*Nu_wave + offset)), 40)
      //Throws out data above nu = 40 or negative

      For(i = 0; i < DimSize(Nu_wave, 0); i += 1)
         If(Nu_wave[i] > 39)
            DeletePoints i, 1, Nu_wave, Long_wave_copy
         Endif
      Endfor

      Interpolate2 /T = 1 /N = (wave_length) /Y = Long_nu Nu_wave, Long_wave_copy
      Duplicate /O Long_nu, Long_nu_adj
   EndIf
```

## B.2 IGOR Plot Output

This code is used to produce an IGOR plot to be exported as a graphics file. The first plot created is minima width as a function of filling factor, and the second is a plot of minima offset as a function of filling factor. "ModifyGraph" commands are IGOR formatting commands to change such parameters as axis scaling, plot trace color, marker style, etc.

```
If(plot_edge_err == 2)
   Wave avs_diffs, edge_nus, avs_upper_error, avs_lower_error, edge_widths
   Wave edge_upper_error, edge_lower_error

   Display avs_diffs vs edge_nus as "Minima Offset vs. Nu"
   ErrorBars avs_diffs Y, wave = (avs_upper_error, avs_lower_error)

   ModifyGraph mode(avs_diffs)=3, marker(avs_diffs)=19, msize(avs_diffs)=2
   ModifyGraph gridRGB=(0,0,0), rgb=(0,0,0), zero(left)=2
   ModifyGraph manTick(bottom)={0,4,0,0}, grid = 0, nticks = 5, tick=2,
   ModifyGraph mirror=1, standoff=0, lowTrip(left)=0.01
   Label left "Offset in \\F'symbol'n\\F'arial'"
   Label bottom "\\F'symbol'n\\F'arial'"
   SetAxis/A/E=0/N=1 left
   SetAxis bottom 0,40
   TextBox/N=myTitle/F=0/A=MC/X=3/Y=48.4/E title

   Display edge_widths vs edge_nus as "Minima Width vs. Nu"
   ErrorBars edge_widths Y, wave = (edge_upper_error, edge_lower_error)

   ModifyGraph mode(edge_widths)=3, marker(edge_widths)=19,
   ModifyGraph msize(edge_widths)=2, tick=2, mirror=1, standoff=0
   ModifyGraph manTick(bottom)={0,4,0,0}, grid = 0, nticks = 5
   ModifyGraph gridRGB=(0,0,0), rgb=(0,0,0), zero(left)=2,lowTrip(left)=0.01
   Label left "WIdth in \\F'symbol'n\\F'arial'"
   Label bottom "\\F'symbol'n\\F'arial'"
   SetAxis/A/E=0/N=1 left
   SetAxis bottom 0,40
   TextBox/N=myTitle/F=0/A=MC/X=3/Y=48.4/E title
EndIf
```

# Bibliography


[1] J. P. Eisenstein, *Am. J. Phys.* **61**, 179 (1993)

[2] J. P. Eisenstein and H. L. Störmer, *Science* **248**, 1510 (1990)

[3] J. H. Davies, *The Physics of Low-Dimensional Semiconductors, an Introduction*, Cambridge University Press, Cambridge (1998)

[4] B. I. Halperin, *Sci. Am.* **254**, 52 (1986)

[5] H. L. Störmer and D. C. Tsui, *Science* **220**, 1241 (1983)

[6] B. I. Halperin, *Phys. Rev. B* **25**, 2185 (1982)

[7] K. B. Cooper, *California Institute of Technology Doctoral Thesis* (2003)

[8] K. Von Klitzing, G. Dorda, and M. Pepper, *Phys. Rev. Lett.* **45**, 494 (1980)

[9] M. Kellogg, J. P. Eisenstein, L. N. Pfeiffer, and K. W. West, *Phys. Rev. Lett.* **93**, 036801 (2004)

[10] J. P. Eisenstein and A.H. MacDonald, *Nature* **432**, 691 (2004)

[11] I. B. Spielman, *California Institute of Technology Doctoral Thesis* (2004)

[12] D. A. Broido and L. J. Sham, *Phys. Rev. B* **31**, 888 (1985)